Full length Article

S-wave velocity structure and site effect parameters derived from microtremor arrays in the Western Plain of Taiwan

Chun-Hsiang Kuo [a,*], Chun-Te Chen [b], Che-Min Lin [a], Kuo-Liang Wen [a,c], Jyun-Yan Huang [a], Shun-Chiang Chang [c]

[a] National Center for Research on Earthquake Engineering, Taipei, Taiwan
[b] Institute of Earth Science, Academia Sinica, Taipei, Taiwan
[c] Department of Earth Sciences, National Central University, Taoyuan, Taiwan

A B S T R A C T

In this study, microtremor array measurements were conducted at 45 sites in the Western Plain of Taiwan. The arrays were approximately 30 m or 60 m in radius, depending on the site. The maximum-likelihood frequency–wavenumber method was adopted to obtain the phase velocities of Rayleigh waves, and then a genetic algorithm technique based on an inversion scheme of the fundamental mode of the Rayleigh waves' dispersion curves was applied to calculate a preliminary S-wave velocity (Vs) profile at each site. Because a layer of thick sediment covers the bedrock in the Western Plain of Taiwan, microtremor arrays in this size range cannot estimate the structure of the entire sediment. Therefore, this study implemented further inversion of the horizontal-to-vertical spectral ratios of the microtremors to estimate the deeper structures up to the bedrock of Vs greater than 1000 m/s. Previously logged velocity profiles for different depths at or near our study sites were collected and compared with the Vs profiles derived from our microtremor array measurements; the results were found to be highly comparable. Therefore, we could delineate the depth distributions for the layer depths for Vs = 600 m/s and 1000 m/s in this region. The depth for Vs = 600 m/s is approximately 50 m in the piedmont area and approximately 300 m at the coastline; moreover, the depths for Vs = 1000 m/s increase from 200 m in the piedmont area to approximately 1000 m at the coastline. The depths for Vs = 1.0 km/s (Z1.0), which is an important parameter that accounts for the basin effect in recent ground motion prediction equations, are consequently available at the study sites. The distribution of Z1.0 as a function of Vs30 indicates higher similarity to that in Japan than in the San Francisco Bay area.

1. Introduction

The Western Plain of Taiwan, which is the largest plain in Taiwan, borders the Western Foothills in the east and the Taiwan Strait in the west. A series of folds and faults in the Western Foothills causes high seismicity and has resulted in numerous destructive earthquakes in this region. Five of the ten most disastrous earthquakes in Taiwan during the past century (1898–1997) occurred in this region: the November 6th, 1904 Touliu Earthquake (M_L 6.1), the March 17th, 1906 Meishan Earthquake (M_L 7.1), the December 17th, 1941 Chungpu Earthquake (M_L 7.1), the December 5th, 1946 Hsinhua Earthquake (M_L 6.1), and the January 18th, 1964 Paiho Earthquake (M_L 6.3) (Cheng et al., 1999). Moreover, immediately after the atlas (Cheng et al., 1999) was published, the well-known Chi-Chi Earthquake (M_L 7.3; M_W 7.6) occurred. Fig. 1 shows the seismicity in this region, indicating the epicenters of the earthquakes with magnitudes greater than 4 that occurred between January 1st, 1900 and December 31st, 2013 (Shin et al., 2013). The six most disastrous earthquakes are denoted by A–F in the order of occurrence. The active faults in this region—the Changhua, Chelungpu, Tamaopu-Shuangtung, Tachienshan, Meishan, Chiuchiungkeng, Chukou, Muchiliao, Liuchia, Houchiali, Hsinhua, Tsochen, and Chaochou faults—are denoted by 1–13, respectively (Central Geological Survey, 2010). Recent studies conducted in Taiwan observed high annual slip rates and a higher probability of seismic hazards across the Changhua, Chelungpu, Meishan, Chiuchiungkeng, and Chukou faults (Rau et al., 2015; Hu et al., 2015). This region is, therefore, considered to have a high probability of being struck by a large earthquake.

Several important cities with major economies and large populations are located in the Western Plain of Taiwan and are therefore

* Corresponding author at: 200, Sec.3, Xinhai Rd., Taipei 10668, Taiwan.
 E-mail address: chkuo@ncree.narl.org.tw (C.-H. Kuo).
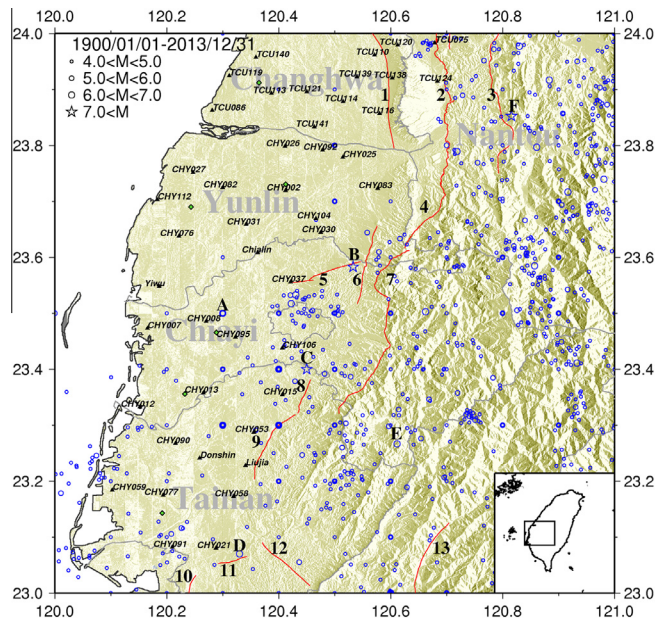
Fig. 1. Historical seismicity with magnitudes greater than 4 in the research area from January 1, 1900 to December 31, 2013. Epicenters are indicated by different sizes and colors of circles. Six disastrous earthquakes are denoted by A–F in the order of date of occurrence. Thirteen active faults are indicated as 1–13. The triangles are the locations of the 45 sites for array measurements in this study. Forty-one of these sites are at the free-field strong-motion stations and are denoted by a code comprising three letters and three numbers, while the remaining four sites, which are schools, are referred to by their names: Chialin, Yiwu, Donshin, and Liuja. The green diamonds indicate the array locations considered by Lin et al. (2009). (For interpretation of the references to color in this figure legend, the reader is referred to the web version of this article.)

threatened by seismic hazards. Simulation and prediction studies of strong ground motions in this region are thus required to reduce the effects of such strong temblors. The Western Plain is covered by a very thick layer of unconsolidated sediment; thus, understanding the shear-wave (S-wave) velocity structures for the sedimentary layers in the region in advance is an essential issue. Velocity logging provides the average S-wave velocity in the top 30 m of the soil (Vs30) at many free-field strong-motion stations in this region (Kuo et al., 2011, 2012). Although Vs30 is a very popular and widely used site parameter in studies involving strong-motion prediction equations, it is insufficient for sites with sedimentary layers greater than 30 m thick, such as those found in the Western Plain of Taiwan. In this study, microtremor array measurements were conducted at 45 sites in the plain and piedmont areas lying at latitudes 23–24° (Fig. 1). To determine the deeper S-wave velocity profiles, 41 of these arrays were located at the same sites as free-field strong-motion stations (elementary schools or junior high schools). The results of such studies are very useful for full-waveform simulations of strong ground motion by considering site effects (Chen et al., 2016).

Following the pioneering work by Aki (1957), Horike (1985) and Matsushima and Okada (1990) established a technique for the determination of S-wave velocity profiles using the microtremor array method. Since then this method has been emphasized as a useful and reliable approach in many studies (e.g., Sato et al., 1991; Kawase et al., 1998; Satoh et al., 2001a, 2001b; Louie, 2001; Kudo et al., 2002; Ohori et al., 2002; Wathelet et al., 2004; Picozzi et al., 2005; Giulio et al., 2006; García-Jerez et al., 2007; Pancha et al., 2008; Lin et al., 2009; Kuo et al., 2009; Raptakis and Makra, 2010; Nardone and Maresca, 2011; Wu and Huang, 2012, 2013). Noninvasive and active source techniques such as Spectra Analysis of Surface Waves (SASW) and Multichannel

Analysis of Surface Waves (MASW) are very popular in estimating S-wave velocity profiles because of the high-frequency vibration source. The microtremor array method, a noninvasive technique, uses a passive source and therefore can detect deeper structures than active source approaches can. The inversion technique of the horizontal-to-vertical spectral ratio (HVSR) of microtremors was proposed in several studies (e.g., Fäh et al., 2003; Arai and Tokimatsu, 2004). A joint inversion scheme that uses both S-wave phase velocities and the HVSR of microtremors was consequently proposed to extend the reliable depth of S-wave velocity profiles and increase the accuracy of inverted S-wave velocity profiles, especially for a depth up to bedrock (Arai and Tokimatsu, 2005; Parolai et al., 2005; Picozzi et al., 2005; García-Jerez et al., 2007).

Varying characteristics of near-surface layers usually cause various amplification effects at strong-motion sites. Vs30 is recommended as an important index for identifying local seismic amplification conditions in modern building codes (e.g., BSSC, 2004). Recently, Vs30 was also emphasized as a significant site parameter in the Ground Motion Prediction Equations (GMPEs) of the Next Generation Attenuation (NGA) projects. However, Vs30 does not explicitly include site response, especially at sites located on thick sediments (Castellaro et al., 2008; Kuo et al., 2015). The depth parameters such as Z1.0 and Z2.5, which are the depths for the S-wave velocities of 1.0 km/s and 2.5 km/s, respectively, were therefore introduced to account for three-dimensional basin effects in GMPEs (Abrahamson and Silva, 2008; Chiou and Youngs, 2008). Measurements of Vs30 are already available in many free-field stations of the Taiwan Strong Motion Instrumentation Program (TSMIP) (Kuo et al., 2012). Z1.0 was derived at the stations investigated by the microtremor array method in the present study and will be helpful for seismic hazard analysis in the Western Plain of Taiwan.

2. Local geology

The regional topography of western Taiwan, shown in Fig. 1, is divided geologically into the Western Plain and the Western Foothills (Ho, 1988). The Western Plain is low, flat, and wide and is the largest plain in Taiwan. A very thick Quaternary unconsolidated sedimentary layer covers the older geological features, which are much more complex than simple sediments. Complex structures such as folds and faults can be found in the Western Foothills, where the sediment thickness is comparatively small. Therefore, the Western Foothills and the nearby Western Plain require greater attention when analyzing seismic hazards. In addition to the six highly disastrous earthquakes mentioned earlier (denoted as A–F in Fig. 1), the 1993 Tapu Earthquake (M_L 5.7) and the 1998 Rueyli Earthquake (M_L 6.2) also destroyed buildings in this region. The Peikang Basement High is a very hard extension of the Eurasian Plain, which acts as a prominent barrier under the central part of the Western Plain. It is located beneath the thick sediment and separates the Neogene sedimentary basins into the Tainan basin in the south and the Taihsi basin in the north (Meng, 1968; Sun, 1982). The existence of this very hard basement is believed to result in the relatively lower seismicity in the plain area at latitudes 23.6–24° as well as several normal faults in east–west strike near Peikang and Meishan.

Thirteen active faults in this region are indicated by the Central Geological Survey (CGS): the Changhua Fault (1), the Chelungpu Fault (2), the Tamaopu-Shuangtung Fault (3), the Tachienshan Fault (4), the Meishan Fault (5), the Chiuchiungkeng Fault (6), the Chukou Fault (7), the Muchiliao Fault (8), the Liuchia Fault (9), the Houchiali Fault (10), the Hsinhua Fault (11), the Tsochen Fault (12), and the Chaochou Fault (13). The fault numbers in the

brackets are denoted in Fig. 1. Faults 1, 2, 3, 4, 5, 7, 9, and 11 are Holocene active faults (the last dislocation was within 10,000 years). The others are Late Pleistocene active faults (the last dislocation was within 100,000 years).

3. Measurements of microtremor arrays

Measurements of microtremor arrays were conducted at the 45 sites (elementary and junior high schools) in the Western Plain of Taiwan located at latitudes 23–24°, as shown in Fig. 1. In addition, 41 of the 45 sites were classified as free-field strong-motion stations by the Central Weather Bureau (CWB). Ten instruments were used for every array measurement and were configured at the center and vertices of triple triangles, as shown in Fig. 2. According to the area of each site, one or two array measurements were conducted. Although the array size varied, the maximum radii of the arrays are broadly categorized as 32, 50, 64, or 96 m, and the minimum radii of the arrays are 2, 3, 4, or 8 m. The actual radii may differ from the expected radii because of obstructions in the field, such as buildings and culverts. The microtremor arrays were measured using portable servo seismometers from Tokyo Sokushin Co., Ltd. Each instrument set consists of a SAMTAC-801B recorder, which is a 24-bit recorder with an MO access device, and a VSE311C or VSE315D sensor, which is a six-channel seismometer (three velocities and three accelerations) with a flat amplitude of 0.07–100 Hz. The internal clock was corrected by a global positioning system before each measurement such that the instruments could make simultaneous observations. The sampling rate was 100 points per second for all microtremor array measurements, while the duration of the measurements was 37 min or 75 min. Fig. 2 shows an example of the configuration of the small (radii 3, 6, and 12 m) and large (radii 12, 24, and 48 m) arrays at station CHY002. The largest radius of the small array is equal to the smallest radius of the large array at the same site in our measurements. The common radius is 12 m in this case. The relative coordinates of the seismometers were measured with

respect to the center instrument using a total station. The open red triangles indicate seismometer records that were not used for further data processing because of abnormal high-frequency noise.

4. Data processing and methodology

4.1. Frequency–wavenumber (F–K) method

Aki (1957) proposed an approach using seismic noise as an effective tool for investigating S-wave velocity structures. He utilized small-scale circular seismic arrays, and derived a phase–velocity dispersion curve by correlating noise records using a spatial autocorrelation (SPAC) method. Capon (1969) proposed a high-resolution method using the maximum-likelihood of frequency–wavenumber (hereafter, the F–K method) to determine the vector velocity of propagating seismic waves of large aperture seismic arrays (LASA). This method provides seismic data to help distinguish between earthquakes and underground nuclear explosions. Later, a Rayleigh wave inversion technique using array records of microtremors was proposed as a useful exploration method for obtaining the S-wave velocity profiles of sedimentary layers (e.g., Horike, 1985). The SPAC and F–K methods are both primary approaches to obtaining the phase velocities of the fundamental Rayleigh waves from microtremor records.

The F–K method was adopted in this study to identify the phase velocities of sedimentary layers with only the vertical component of the microtremor data obtained from the array measurements. The F–K method assumes that random horizontal plane waves are propagating through the array of sensors on the surface. At a given frequency and wavenumbers k_x and k_y in the x and y directions, respectively, the relative arrival time for each sensor was calculated and the phases were subsequently shifted according to the delay time. Consequently, a power spectrum was derived from the stacked waves. The location of the maximum value of the power spectrum in the (k_x, k_y) plane gives the velocity and the azimuth of the propagating wave through the array. Fig. 3 shows an
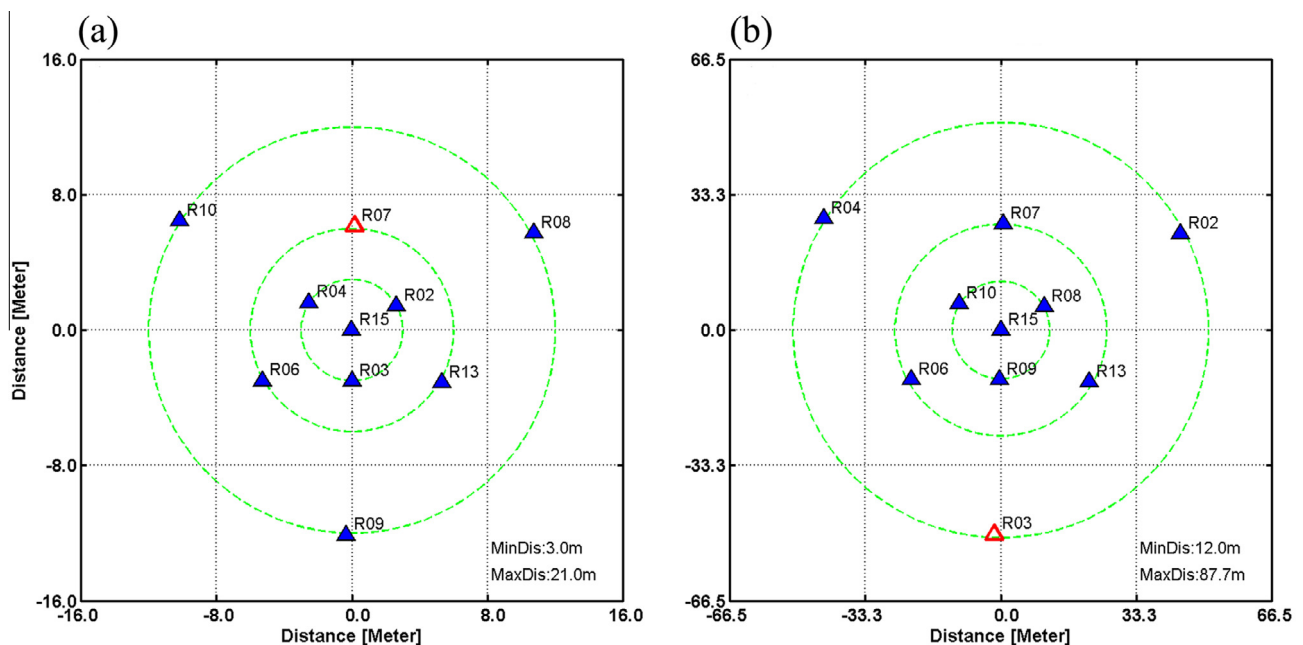

Fig. 2. An example of the configuration of small and large arrays at station CHY002. (a) Configuration of the small array at CHY002. (b) Configuration of the large array at CHY002. Ten instruments were used in every single array measurement and were configured at the center and the vertexes of triple triangles. The open red triangles indicate the locations of unused recordings due to abnormal signals. (For interpretation of the references to color in this figure legend, the reader is referred to the web version of this article.)
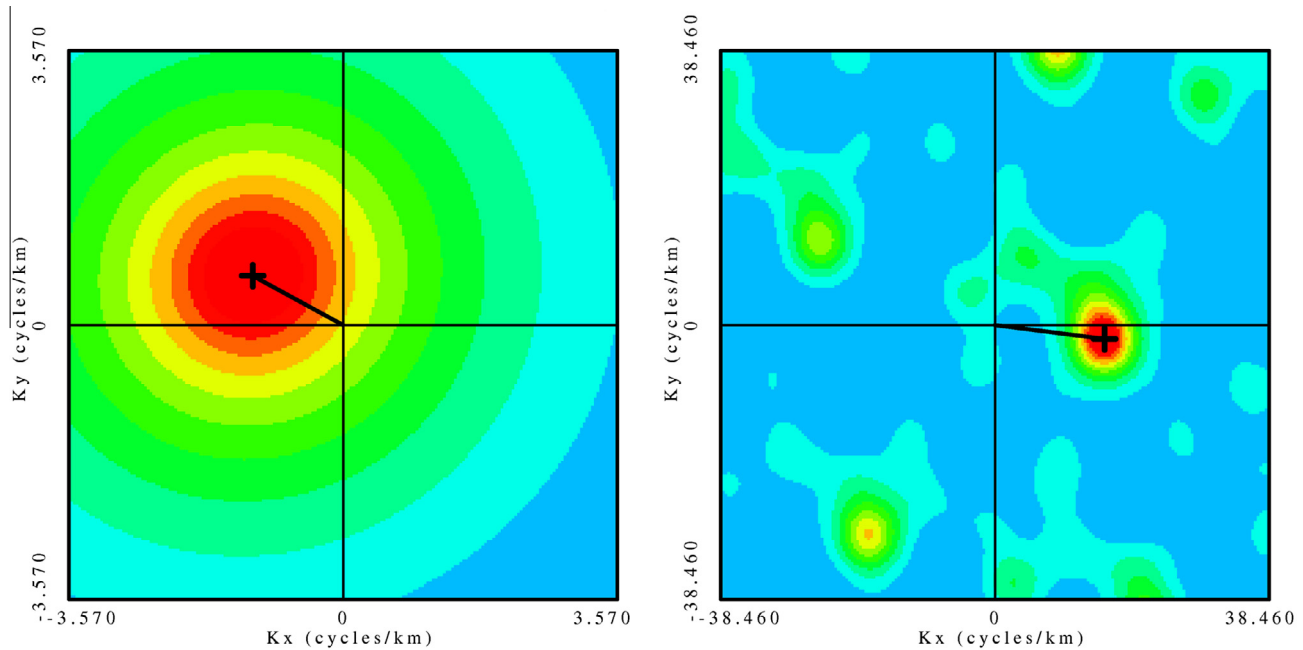
Fig. 3. An example of calculated F–K spectra at frequencies of 1 Hz (left) and 5 Hz (right). Phase velocities were calculated from the resultant wavenumber of the maximum peak and the corresponding frequency of the F–K spectra. The Kx, Ky, velocity, and azimuth are −1.18 cycle/km, 0.64 cycle/km, 0.73 km/s, and 298.6° at 1 Hz, and are 15.4 cycle/km, −1.92 cycle/km, 0.32 km/s, and 97.1° at 5 Hz, respectively.

example of the F–K spectra at frequencies 1 Hz and 5 Hz. Phase velocities were calculated from the resultant wavenumber of the maximum peak and the corresponding frequency of the F–K spectra. The moving window technique with a variable window length for different sizes of arrays was utilized on the vertical component of the microtremor records to calculate the F–K spectra in 101×101 grid points in the wavenumber domain for each frequency.

The average phase velocities obtained by the F–K method at each station are shown in Fig. 4. The 45 stations were distributed from the foothills to the coastline of the research area in order to understand the variation of sedimentary thickness and the characteristics of the S-wave velocity in the entire region. Therefore, the phase velocities from the dispersion curves are categorized into plain and piedmont sites, which are plotted as thin black dashed lines and thick blue lines, respectively, as shown in Fig. 4. The piedmont sites are TCU110, TCU120, TCU075, TCU124, TCU138, TCU116, CHY025, CHY083, CHY037, CHY106, CHY015, CHY053, CHY058, CHY021, and LIUJIA. Several piedmont sites obviously have higher and steeper phase velocities than the plain sites, indicating that the sediments are relatively thinner than those belonging to the plain sites because these sites are located very close to the mountains. The black dispersion curves of the plain sites show similar phase velocities, especially at frequencies higher than 2.5 Hz. This indicates that the lateral variations in S-wave velocity at the piedmont sites are relatively larger than those at the plain sites in the Western Plain of Taiwan.

4.2. Genetic algorithm grid search for dispersion curves

A genetic algorithm (GA) is a powerful forward search technique for computing a global optimum solution and is different from a traditional inversion method. Yamanaka and Ishida (1996) proposed a modified GA inversion method that uses a GA search technique to prepare appropriate initial models for follow-up linear inversions, thereby improving the precision and quality of estimation. Therefore, in this study, we adopted a GA combined
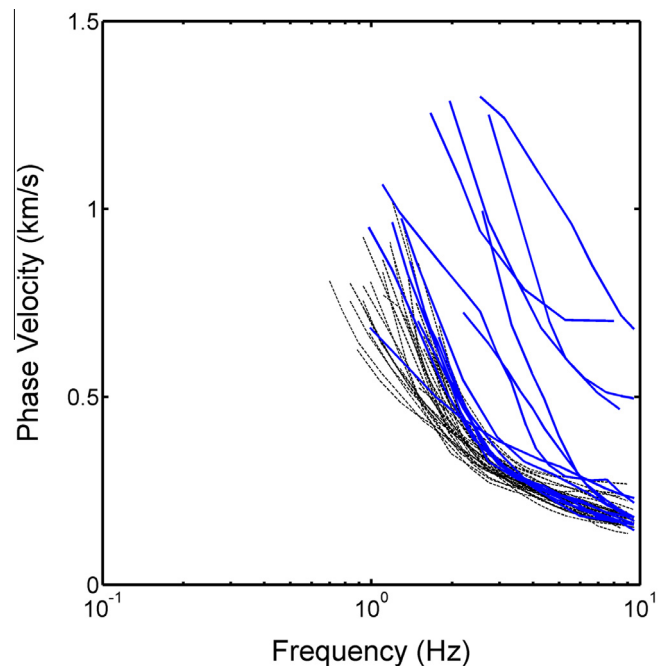
Fig. 4. Dispersion curves of phase velocities obtained by the F–K method at the study sites. The obtained dispersion curves in the plain area (30 sites) and the piedmont area (15 sites) are plotted as black thin dash and blue thick lines, respectively. (For interpretation of the references to color in this figure legend, the reader is referred to the web version of this article.)

with the forward modeling of surface waves proposed by Herrmann (1985) to search for the appropriate initial models within a given range of unknown parameters. The algorithm consists of several modules corresponding to evolution functions, such as reproduction, crossover, selection, and mutation, based on which individuals of a population can be evaluated both globally and locally to obtain an optimal solution.

In this study, a model with eight layers covering a half space is assumed for the GA search for two unknown parameters, S-wave velocity and layer thickness. P-wave velocities and the layer densities were determined on the basis of a simple relation with the S-wave velocities. The population size of each generation was set to 40 and each GA search was terminated at the 450th generation. To increase the variety of optimal solutions, a complete GA process at a site included 30 single GA searches. Consequently, the total number of repetitions was 540,000 for one complete forward modeling. In addition, a fitness function was used for each individual in the GA search selection. A fitness function should be able to determine how a model interprets the observed data. An individual with a larger fitness value has a higher probability of being included in the subsequent generation, thus ensuring good genes are easily transmitted. We adopted a root mean square error (RMSE) type of fitness function (Lin et al., 2009) given by the following equation:

$$RMSE = \sqrt{\frac{1}{n}\sum_{i=1}^{n}(C_{obs}(i) - C_{sim}(i))^2} \qquad (1)$$

where n is the number of observed phase velocities; C_{obs} and C_{sim} are the ith observed and simulated phase velocities, respectively. The fitness function (F_{DC}) is therefore defined as

$$F_{DC} = \left(\frac{1}{1 + RMSE}\right)^{10} \qquad (2)$$

and takes a value between 0 and 1.

4.3. Inversion of the dispersion curve

We attempted to search all possible interfaces that affect the dispersion curves using the GA technique. Therefore, the velocity and thickness range is wide and the assumed number of layers (eight) may be excessive for the observed dispersion curves to be estimated. To counter this drawback, we used the stochastic least squares inversion of the fundamental Rayleigh waves (Herrmann, 1987) after the GA search for dispersion curves. The well-known SURF program, proposed by Herrmann (1987), was used to test the sensitivity of each layer of the S-wave velocity model derived from the GA search. Immaterial layers with insufficient resolutions for the observed dispersion curve were examined and removed. In addition, in this step, we used suitable P-wave velocities and densities according to the estimated S-wave velocities for soil and rock layers to make an adjustment for the models obtained from the GA search. As a result, the observed dispersion curve could be expressed well by the major interfaces of a velocity profile with least variance.

Lin et al. (2009) also used both the GA grid search and the inversion of the dispersion curve using the SURF program to derive the S-wave velocity structures at seven sites in the Western Plain of Taiwan. Six of these sites were located in the same region as the present study as shown in Fig. 1. The maximum radius of their microtremor arrays was approximately 1000 m; therefore, the resolution depth was >2 km.

4.4. GA grid search for the HVSR of microtremors

Since Nakamura (1989) proposed the HVSR method to calculate a transfer function for seismic noise, microtremor measurements for single station have been widely used to assess site responses such as the resonant frequency and amplification factor (Field and Jacob, 1993; Lermo and Chavez-Garcia, 1993). Nakamura (1989) considered that seismic noise tends to induce Rayleigh waves in the vertical component because the surface artificial sources have mostly prevailing vertical motion. The fundamental resonant frequency of the HVSR depends on the thickness and velocity of the sedimentary layers covering the bedrock. Accordingly, in previous studies, the HVSRs of microtremors were simulated for S-wave velocity profile inversion based on the theoretical transfer function of the S-wave (Nakamura, 2007; Lin et al., 2014) or surface waves (Fäh et al., 2003). A joint inversion
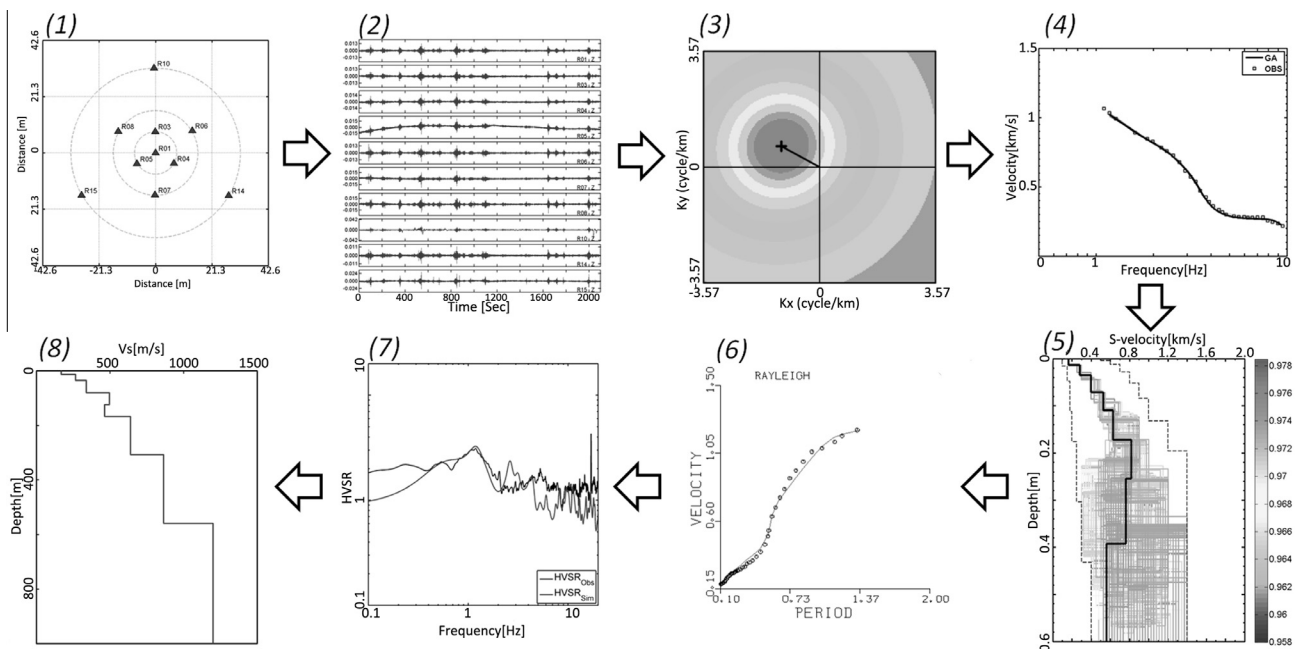
Fig. 5. Illustration of the procedure of the microtremor array method adopted in this study. (1) Array measurements of microtremors, (2) baseline correction of vertical velocity recordings, (3) F–K spectral analysis, (4) observed phase velocities and synthetic dispersion curves, (5) inversion of S-wave velocity profiles using the GA technique, (6) further inversion of dispersion curves using the SURF program, (7) the second stage of inversion of the HVSR, and (8) the final S-wave velocity profile that includes the bedrock with velocities greater than 1000 m/s.

scheme of both phase velocities and the HVSR of microtremors was therefore proposed to extend the reliable depth of the S-wave velocity profile and increase the accuracy of the estimated S-wave velocity profile, especially for depths up to the bedrock (Arai and Tokimatsu, 2005; Parolai et al., 2005; Picozzi et al., 2005; García-Jerez et al., 2007).

Many arrays deployed in this study were not able to acquire the phase velocities of the bedrock because of the large unconsolidated sediment in this region. However, the velocities and thicknesses of all sediments covering the bedrock are important not only for the numerical simulation of seismic waves but also for strong ground-motion predictions. Using a 3D finite-difference simulation, Lee et al. (2008) found that the near-surface Songshan Formation with low S-wave velocity can significantly amplify seismic waves propagating in the Taipei Basin.

The GA technique was again integrated with the theoretical SH-wave transfer function of the Haskell–Thomson matrix (Haskell, 1960), which is derived from the estimated S-wave velocity profiles. Subsequently, a linear correlation coefficient shown in Eq. (3) was used for developing the fitness function of the HVSR (Lin, 2009).

$$r = \frac{\sum_{i=1}^{n}(x_i - \bar{x})(y_i - \bar{y})}{\left[\sum_{i=1}^{n}(x_i - \bar{x})^2 \sum_{i=1}^{n}(y_i - \bar{y})^2\right]^{1/2}} \quad (3)$$

where r is the linear correlation coefficient with a value between -1 and 1; $\bar{x}$ and $\bar{y}$ are the means of observations (x_i) and synthetics (y_i), respectively. A new fitness function was designed as follows:

$$F_{HVSR} = \left(\frac{1+r}{2}\right) \times 0.8 + \left(1 - \frac{|F_{sim} - F_{obs}|}{0.3 \times F_{obs}}\right) \times 0.2 \quad (4)$$
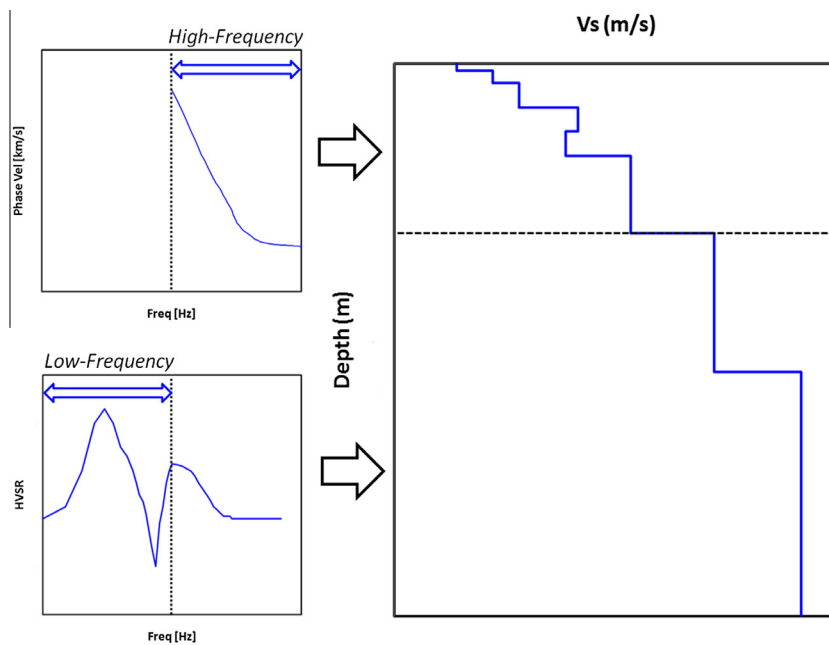
Fig. 6. Schematic illustration of the two-stage inversion scheme. The first stage is the inversion of phase velocities for deriving the shallow part S-wave velocity profile. The second stage is the inversion of the HVSR for obtaining the deep part S-wave velocity profile.
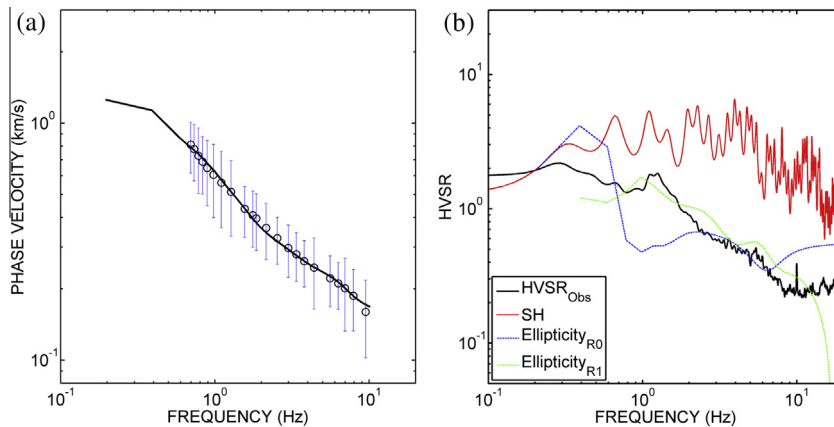
Fig. 7. The observed and simulated results of (a) dispersion curve and (b) HVSR at station CHY112. (a) The observed phase velocities are plotted as black open circles with standard deviations as blue lines; the simulated dispersion curve is plotted as a black line. (b) The observed HVSR is plotted as a black curve; the simulated SH-wave transfer function is plotted as a red curve; the simulated ellipticity for the fundamental mode Rayleigh waves is plotted as a blue dotted curve; and the simulated ellipticity for the first higher mode Rayleigh waves is plotted as a green dotted curve. (For interpretation of the references to color in this figure legend, the reader is referred to the web version of this article.)
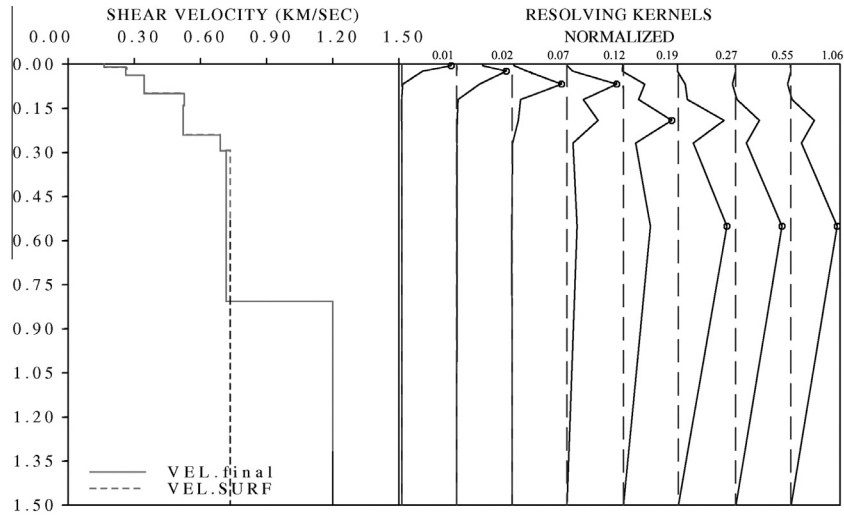
Fig. 8. Final S-wave velocity structures (solid line) and that estimated by SURF (dash line) at CHY112 are shown in the left. The right is the normalized resolving kernel functions at given depths as indicated by the numbers on the top of each function.
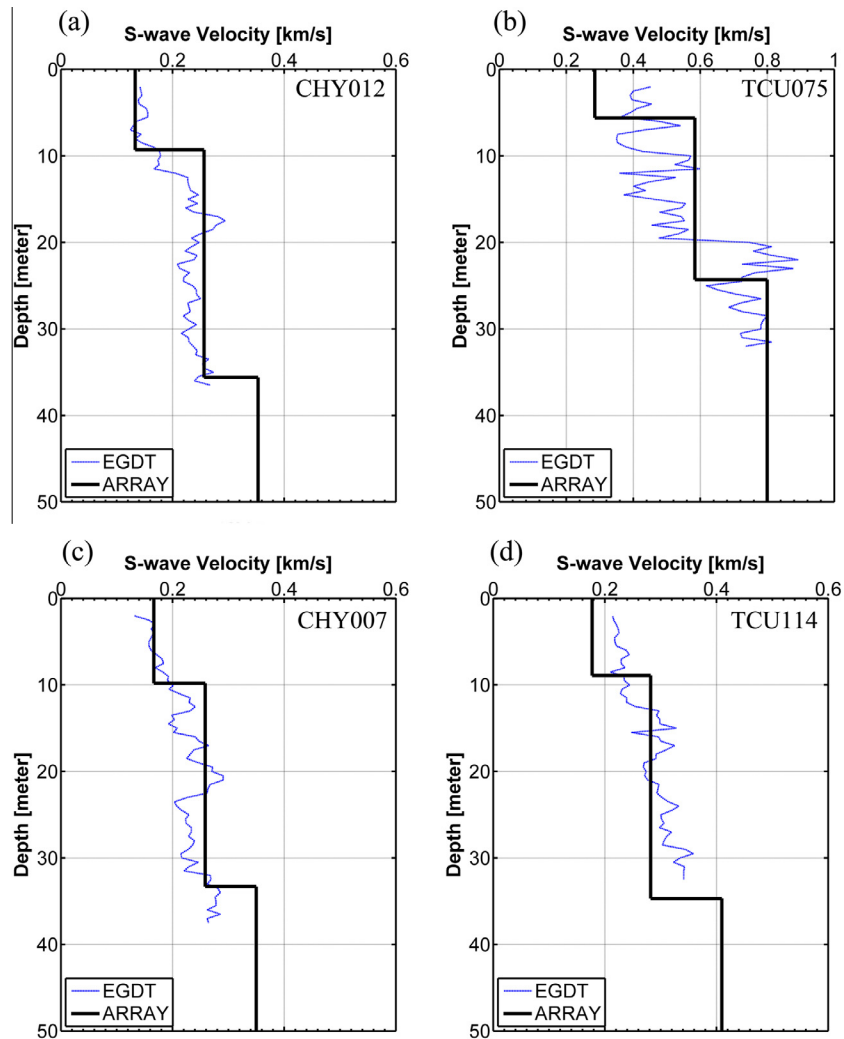

Fig. 9. Comparisons of the S-wave velocity profiles derived by the microtremor array method and the logged S-wave velocity profiles from EGDT for very shallow parts of depths less than 40 m at (a) CHY012, (b) TCU075, (c) CHY007, and (d) TCU114. The thick black line and thin blue line denote the array and logged profiles, respectively. (For interpretation of the references to color in this figure legend, the reader is referred to the web version of this article.)

where F_{sim} and F_{obs} are the dominant frequencies of the simulated transfer function and the observed HVSR, respectively. The fitness of the dominant frequency, which accounts for the sedimentary thickness, can therefore be controlled. This combined method of GA and SH-wave transfer function was used to directly estimate the velocity structure by simulating dense microtremor HVSRs to obtain a detailed model of the layered S-wave velocity for the Taipei Basin (Lin et al., 2014). The population size of each generation was set to 50 and the GA search of the HVSR was terminated at the 450th generation. The velocity ranges of deeper layers as well as the bedrock were obtained from the results of Lin et al. (2009), whereas the thicknesses were estimated by the GA search of the HVSRs.

5. Results and discussions

In this study, we proposed a two-stage inversion scheme of the phase velocity dispersion curve and the HVSRs of microtremors. The basic idea is that in the first stage, the shallower part of the S-wave velocity profiles will be derived from the observed phase velocities, which provide information about both velocities and layer thicknesses, while in the second stage, the deeper part can be estimated from the HVSR, which is related to the sedimentary thickness and the velocity impedance between the sediments and the bedrock. Note that the second stage of inversion was performed under the constraint of the S-wave velocity profile obtained from the first stage of inversion being fixed as the shallow part of the model for estimating the deeper S-wave velocity profiles up to the bedrock. Consequently, the dominant frequency of the HVSR is assumed to be caused by the interface between the sediment and the bedrock in this study. Therefore, the second stage of inversion was applied except for six sites (CHY025, TCU075, TCU116, TCU120, TCU124, and TCU138) as their bedrock (S-wave velocity greater than 1000 m/s) was derived from the obtained phase velocities in the first stage of inversion.

The procedure of the microtremor array method adopted in this study is shown in Fig. 5. The following steps are involved: (1) microtremor array measurements, (2) vertical velocity recordings after baseline correction exhibiting similar signals in all velocity traces, (3) F–K spectral analysis, (4) observed phase velocities and synthetic dispersion curves, (5) inversion of S-wave velocity profiles using the GA technique, (6) further inversion of dispersion curves to check the essentiality of each layer using the SURF program, (7) second stage inversion of the HVSRs of microtremors, and (8) the final S-wave velocity profiles that include bedrock velocities greater than 1000 m/s. A schematic representation of the two-stage inversion scheme is shown in Fig. 6. The first stage is the inversion of phase velocities, which derives the shallow part
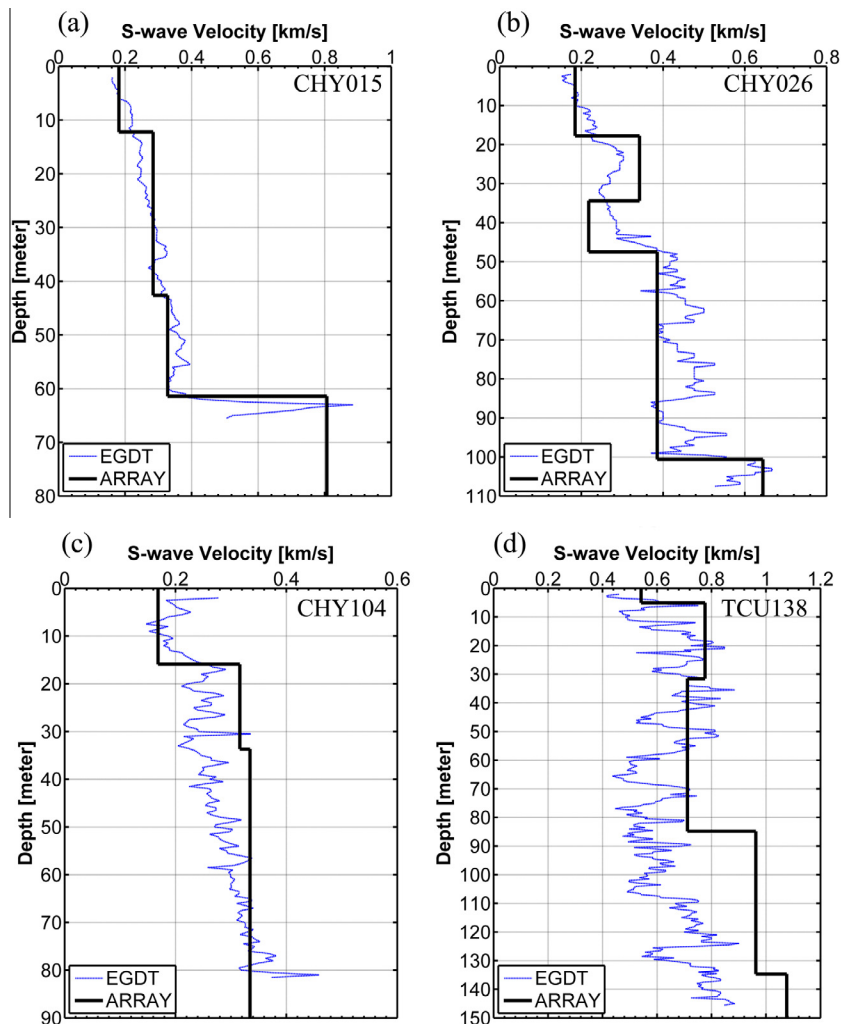
Fig. 10. Comparisons of the S-wave velocity profiles derived by the microtremor array method and the logged S-wave velocity profiles from EGDT for depths of 50–150 m at (a) CHY015, (b) CHY026, (c) CHY104, and (d) TCU138. The thick black line and thin blue line denote the array and logged profiles, respectively. (For interpretation of the references to color in this figure legend, the reader is referred to the web version of this article.)
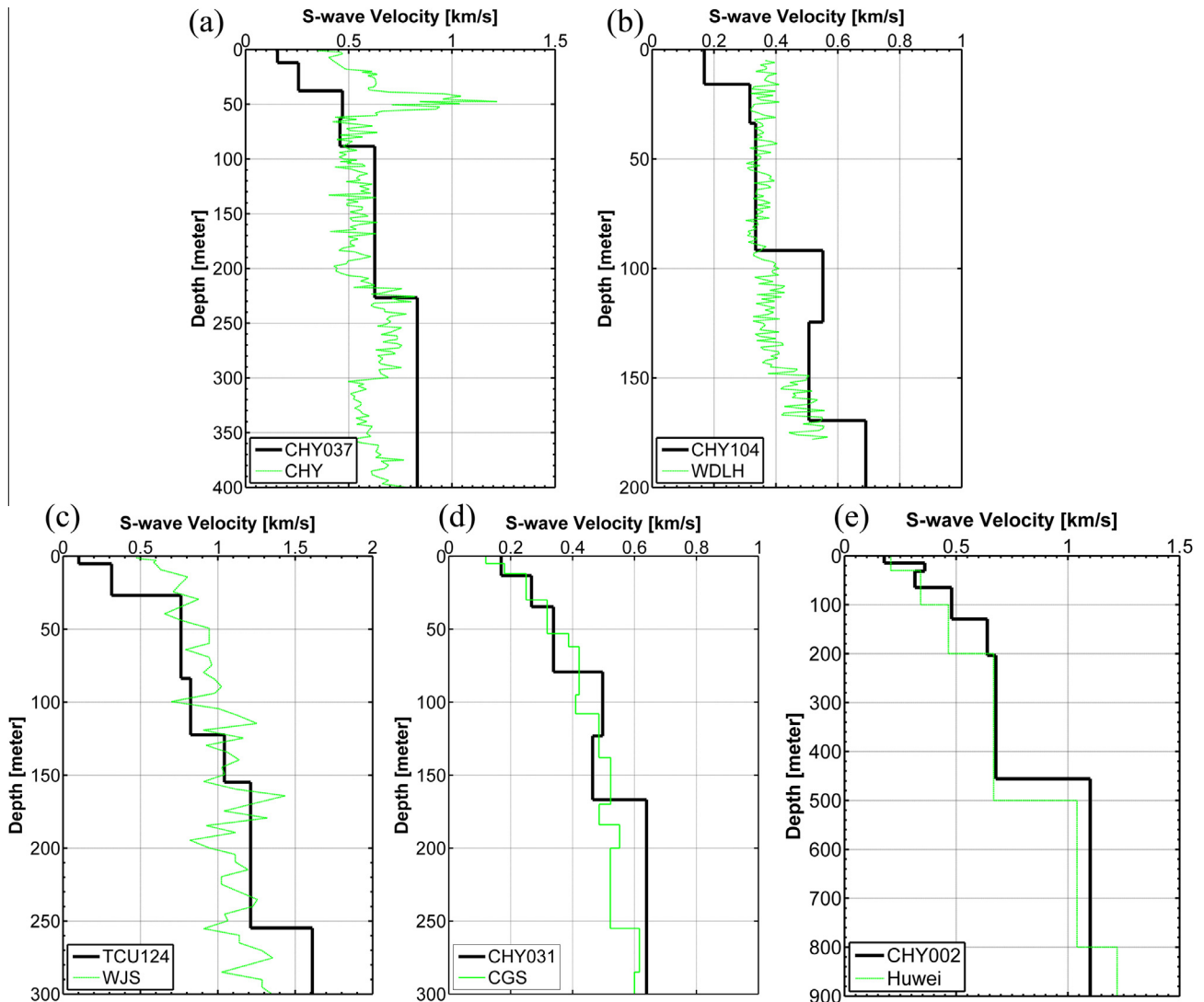
of the S-wave velocity profiles. Furthermore, the second stage is the inversion of the HVSR, which derives the deep part of the S-wave velocity profiles.

Fig. 7 shows an example of the inversion results for the site CHY112. The observed phase velocities and HVSR as well as the simulated results using the final Vs model are shown as Fig. 7a and b, respectively. The observed phase velocities are shown as black open circles with the standard deviations indicated by blue lines. The simulated dispersion curve fits the observations quite well. The observed HVSR and the simulated SH-wave transfer function curves are plotted in black and red; the simulated ellipticity of the fundamental mode Rayleigh waves is plotted as a blue dotted curve; and the simulated ellipticity of the first higher mode Rayleigh waves is plotted as a green dotted curve. The fitness of the simulated SH-wave transfer function, the ellipticity of Rayleigh waves, and the observed HVSR is acceptable for the dominant frequency at around 0.3 Hz, which accounts for the thickness of the unconsolidated sediments. However, for higher frequencies, the theoretical SH-wave transfer function usually shows a higher amplitude than that of the microtremor HVSR as indicated in many studies (e.g., Guillier et al., 2005; García-Jerez et al., 2006).

Otherwise, the ellipticity of the fundamental mode Rayleigh wave shows a comparable dominant frequency and first trough (~1 Hz). The ellipticity of the first higher mode further fits the second peak and the portion of the HVSR from 1 Hz to 10 Hz. The successful inversion of the HVSR resultant Vs profile extends to the bedrock, and thus, the simulated dispersion curve (the black line in Fig. 7a) exhibits a significant trend at the lower frequency than the observed phase velocities. Resolving kernel functions, the final S-wave velocity structure and the S-wave velocity model derived by SURF for CHY112 are shown in Fig. 8. The shallow part of the S-wave velocity structure is well resolved by the dispersion velocities.

5.1. Comparison with logging results

Velocity profiles measured by a suspension PS-logging approach at many free-field strong-motion stations in Taiwan are available from the Engineering Geological Database for TSMIP (EGDT) by the cooperative efforts of the National Center for Research on Earthquake Engineering (NCREE) and the CWB (Kuo et al., 2012). Most of these velocity profiles have depths of around 35 m, while several velocity profiles have depths greater than

Fig. 11. Comparisons of the S-wave velocity profiles derived by the microtremor array method and the logged S-wave velocity profiles from CWB and CGS for depths of 170–400 m at (a) CHY037, (b) CHY104, (c) TCU124, and (d) CHY031. Otherwise, the comparison of results at CHY002 and Huwei (Lin et al., 2009) for a depth up to 900 m is shown at (e). The thick black line and thin green line denote the array and logged profiles, respectively. (For interpretation of the references to color in this figure legend, the reader is referred to the web version of this article.)

50 m. The CWB recently started installing surface-downhole seismic stations, which provide velocity profiles with a depth of greater than 300 m at several stations. Three of these stations are located in the research area and hence logged velocity profiles by suspension PS-logging method were available. We also collected another velocity profile with a depth of 300 m from a report by the CGS (2007). We compared these logged velocity profiles with the velocity profiles derived by the microtremor array method in this study in order to verify the accuracy of our results.

For the very shallow part with a depth less than 40 m, the derived S-wave velocity profiles using microtremor array measurements were compared with the logged profiles from the EGDT at four sites, CHY012, TCU075, CHY007, and TCU114, as examples (Fig. 9). In the figure, the microtremor array results are plotted as thick black lines and the logged data are plotted as blue lines. Both results are very similar to each other at all the four sites, indicating that the microtremor array measurements are highly accurate for the very shallow part. For depths of approximately 50–150 m, the measurements for the four sites, CHY015, CHY026, CHY104, and TCU138, were taken as examples and shown in Fig. 10. Except for the deeper part at TCU138, the microtremor array results are similar to the logged S-wave velocity profiles. At TCU138, both velocity profiles show a slight velocity decrease at depths of 30 m (array) and 40 m (EGDT) and then again an increase at depths of 85 m (array) and 110 m (EGDT). To confirm the validity of the results of the velocity profiles for medium depths (~300 m) derived in this study, the logged S-wave velocity profiles from three CWB surface-downhole seismic stations, CHY, WDLH, and WJS (Wen et al., 2014), are considered. Fig. 11a shows the comparison of the logged result at station CHY (green line) and our array measurement result at CHY037 (thick black line). CHY037 is the closest site to the station CHY in this research. A divergence is observed at the shallow and deep parts between the two profiles. A comparison between the S-wave velocity profiles obtained from the microtremor arrays and the logged result at station CHY can be found in Fig. 9 of Wu and Huang (2013). The S-wave velocity profiles from the microtremor arrays showed relatively lower values at a depth less than 65 m and relatively higher values at a depth larger than 280 m. In fact, the S-wave velocity profiles obtained by the microtremor arrays at CHY resemble our microtremor array results although there is a distance of 5 km between the two sites. The logged profile at WDLH was comparable to our microtremor array results at CHY104 within a depth of approximately 175 m (Fig. 11b). Fig. 11c shows the comparison between the logged profile at WJS and our microtremor array result at TCU124 for a depth within 300 m. The obvious discrepancy at the very shallow part with depths less than 25 m may be because of the horizontal distance of about 10 km between the two sites. In addition, we also considered a logged velocity profile obtained from a technical report of CGS (2007) at the same elementary school at CHY031. Fig. 11d shows the CGS logged S-wave velocity profiles and our microtremor array result at CHY031. The profiles are highly comparable within a depth of 300 m. Otherwise, CHY002 and the Huwei site of Lin et al. (2009) are close to each other, and thus, the resultant S-wave velocity profiles are plotted together in Fig. 11e. The S-wave velocity structures at CHY002 and Huwei are quite similar up to a depth of 900 m. The comparisons with logged results at different depth ranges (40 m, 150 m, and 400 m), as described above, confirm that the S-wave velocity profiles derived by the microtremor array method using a two-stage inversion scheme in this study are highly reliable.

5.2. Update of Vs30 map

Vs30 is a significant parameter accounting for site effects and has been used widely in GMPEs and building codes (BSSC, 2004;
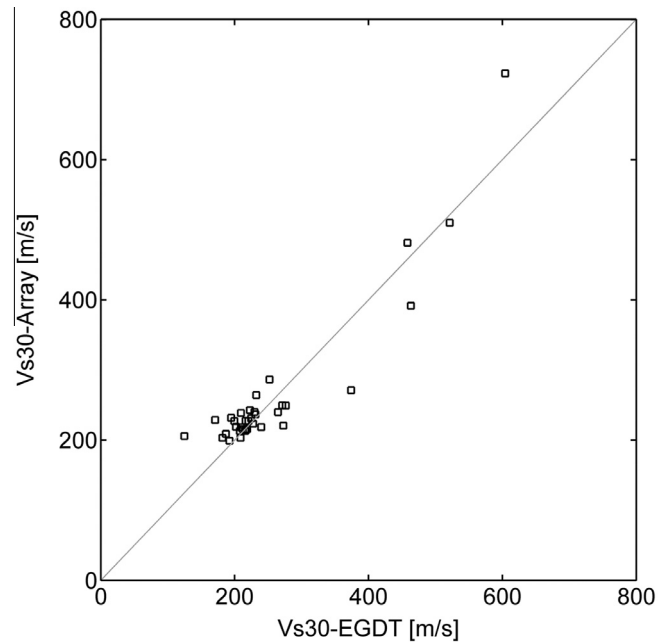

Fig. 12. Comprehensive comparison of the Vs30 values obtained from logged data from the EGDT (x-axis) and from the microtremor array result in this study (y-axis).

ASCE, 2010). Fig. 12 shows a comparison of Vs30 calculated from the S-wave velocity profiles derived from microtremor arrays (y-axis) and that obtained from the EGDT (x-axis). Most of the microtremor array measurements were conducted in the plain area, and so most Vs30 values are less than 300 m/s. Little inconsistency is observed between the Vs30 values obtained from the two approaches, thus confirming the accuracy of the microtremor array measurements in the entire research region. Consequently, Fig. 13
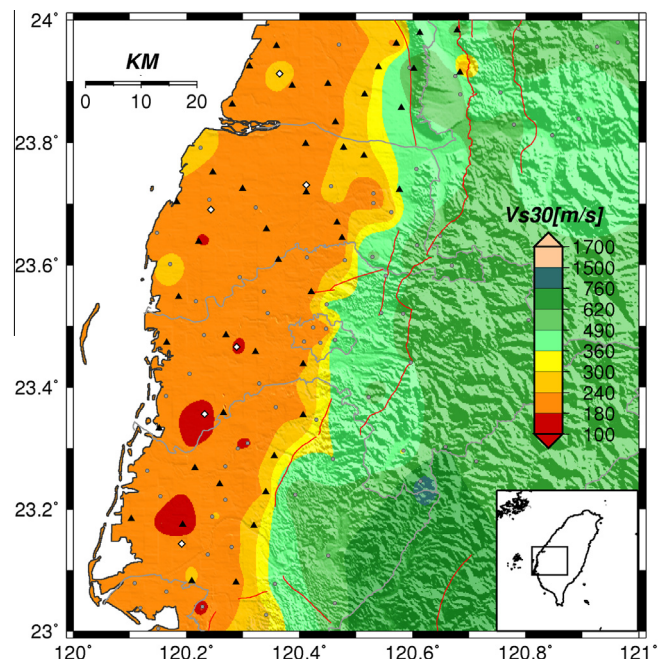

Fig. 13. Updated Vs30 map for the Western Plain of Taiwan using results of both the EGDT (gray circles) and microtremor array measurements. The black triangles and white diamonds indicate the locations of microtremor arrays in the present study and in Lin et al. (2009), respectively.

shows the integration of the Vs30 obtained from the EGDT (gray circles), our S-wave velocity profiles (black triangles), and the S-wave velocity profiles from Lin et al. (2009) (white diamonds) to illustrate a Vs30 map for the Western Plain of Taiwan. Vs30 values of 180–240 m/s are shown in most areas of the plain, as shown in Fig. 13. Several sites with slightly higher or lower Vs30 are also scattered on the plain. Higher Vs30 values of 490–760 m/s are observed in the mountain area, whereas Vs30 values of 240–490 m/s are mostly distributed in the narrow piedmonts.

5.3. Depth contours of Z0.6 and Z1.0

To understand the distribution of important bedrock in the Western Plain of Taiwan, we collected the results of the seven large microtremor arrays from Lin et al. (2009). In fact, the velocities of the deep layers used in the second-stage inversion in our study were referring to the results of Lin et al. (2009), as described in the section GA Grid Search for the HVSR of Microtremors. By using the S-wave velocity profiles from the 51 microtremor array measurements, the depth contours of the bedrocks with S-wave velocities 600 m/s and 1000 m/s are delineated as shown in Fig. 14. The depth of the engineering bedrock for Vs = 600 m/s is approximately 50 m in the piedmont area and approximately 300 m in the coastline; moreover, the depth for Vs = 1000 m/s increases from 200 m in the piedmont to approximately 1000 m in the west coast. Several previous studies analyzed the dispersion curves of surface waves generated by large earthquakes in this region (Chung and Yeh, 1997; Hwang et al., 2003), and microtremor array measurements were adopted in Chiayi County of this region (Wu and Huang, 2013). These studies showed similar results on sedimentary thickness distribution. Hwang et al. (2003) showed a sedimentary thickness of about 1 km for Vs < 1000 m/s in their 3rd region (i.e., the western plain), similar to our result; however, our result indicates a thicker sediment in the eastern part compared with their result (the 2nd region). Chung and Yeh (1997) found a sedimentary thickness of about 300 m in their AV2 region, similar to our result; however, our result indicates thicker sediment in the western part compared with their result (AV1 region). The two previous studies used the recordings of strong-ground-motion stations with large distances

between stations, and hence, the resolution for shallow (depth < 1 km) S-wave velocity profiles is not as high as that achieved in this study. Our results are similar to those of Wu and Huang (2013) in Chiayi County in term of the layers with S-wave velocities of 600 m/s and 1000 m/s, the so-called Z0.6 and Z1.0. Z0.6 is less than 100 m in eastern Chiayi City and larger than 300 m in the coastline area; Z1.0 is approximately 300 m in eastern Chiayi City and approximately 900 m at the coastline area. Their depths at the coastline area are less than those in our study because several of our sites are closer to the coastline. The distribution of the dominant frequencies estimated from the HVSR of the microtremors at all 45 stations is illustrated in Fig. 15. This figure
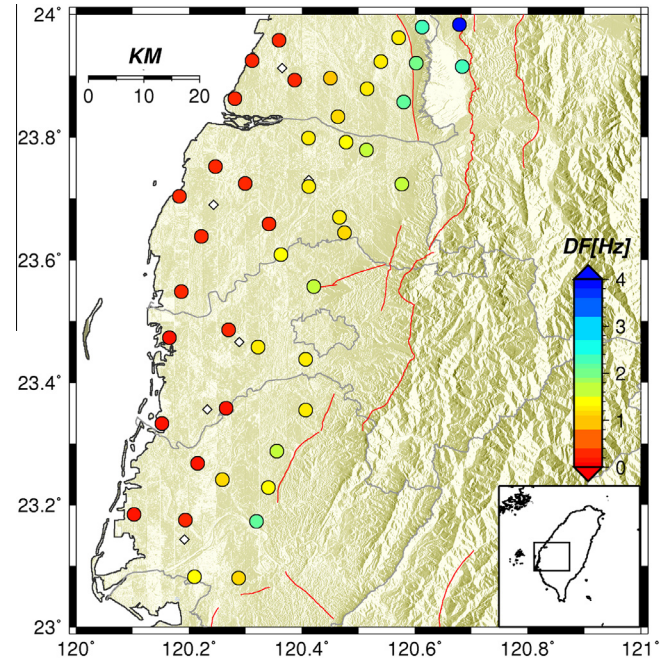

Fig. 15. Distribution of the dominant frequencies estimated from the HVSR of the microtremors at the 45 stations (black triangles). The white diamonds indicate the arrays of Lin et al. (2009).
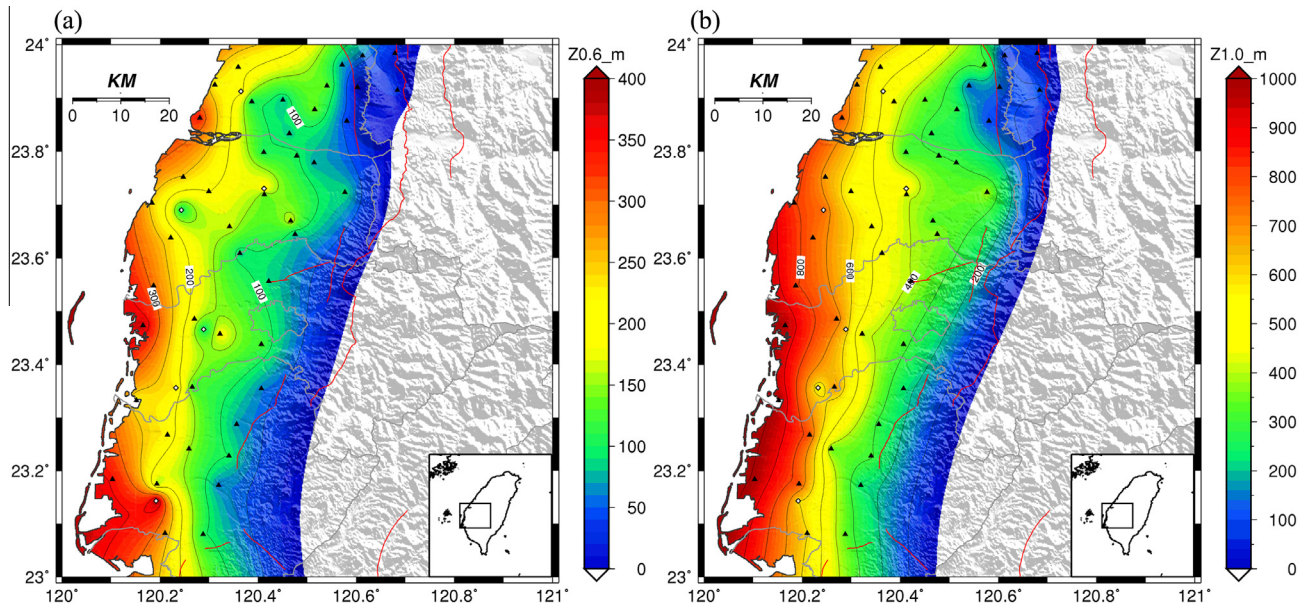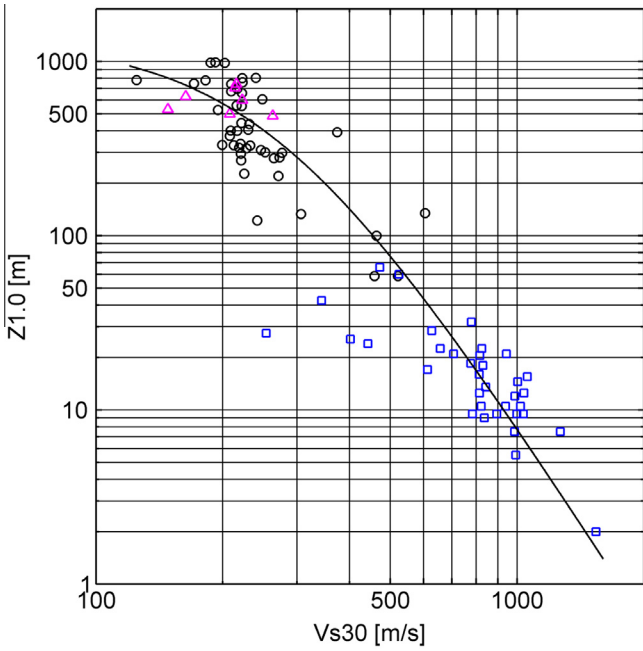

Fig. 14. Depth contour maps for the bedrock with S-wave velocities of (a) 600 m/s and (b) 1000 m/s derived from the results of this study and of Lin et al. (2009). Intervals of the contours are 50 m and 100 m in the two figures.

Fig. 16. Distribution of the Vs30–Z1.0 data obtained from the results of this study (black open circles), Lin et al. (2009) (magenta open triangles), and EGDT (blue open squares); the developed relation is indicated by the black line. (For interpretation of the references to color in this figure legend, the reader is referred to the web version of this article.)

Fig. 17. Locations of the sites that provided the Vs30–Z1.0 data through the measurements of microtremor arrays (black circles: this study; red triangles: Lin et al. (2009)) and EGDT logging (blue squares: Kuo et al. (2012)). (For interpretation of the references to color in this figure legend, the reader is referred to the web version of this article.)
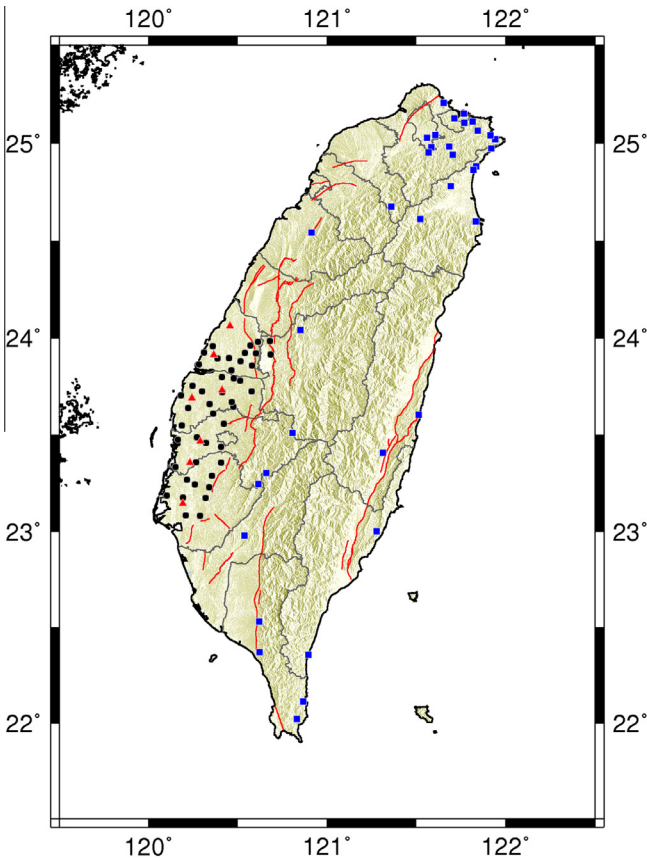
reveals that the dominant frequencies are lower than 1 Hz near the coast line, approximately 1–2 Hz in other plain area, and higher than 2 Hz at the piedmonts.

5.4. Relation between Vs30 and Z1.0 for Taiwan

To account for the basin effect in GMPEs, Abrahamson and Silva (2008) and Chiou and Youngs (2008) recommended using the relation between Vs30 and Z1.0 in the estimation of the parameter Z1.0 at a station for which this parameter is not available. Recently, Abrahamson et al. (2014), Boore et al. (2014), and Chiou and Youngs (2014) used Z1.0 in their GMPEs for NGA-West2. Since Z1.0 has become an important site parameter in recent studies of GMPEs, it is also necessary to provide a Vs30–Z1.0 relation for Taiwan, following the form proposed by Chiou and Youngs (2014). The relation was developed using the results from this study (black open circles), Lin et al. (2009) (magenta open triangles), and the EGDT (blue open squares) as shown in Fig. 16. The Vs30–Z1.0 data from the microtremor array measurement on the Western Plain of Taiwan provided knowledge of soft and stiff soil sites (black circles and red triangles in Fig. 17, respectively); the data from EGDT provided knowledge of soft soil, stiff soil, and rock sites (blue squares in Fig. 17). A complete distribution of Vs30–Z1.0 was therefore integrated. The data distribution for Taiwan, shown in Fig. 16, is more similar to that for Japan than for California (Chiou and Youngs, 2013); therefore, the Japan's equation was selected for Taiwan:

$$\ln(Z_{1.0}) = \frac{-3.8}{2}\ln\left(\frac{V_{s30}^2 + 266^2}{1750^2 + 266^2}\right) \qquad (5)$$

The units for Z1.0 and Vs30 are m and m/s, respectively. The functional form of Eq. (5) was selected to follow the trend of available Vs30–Z1.0 data in Taiwan. Fig. 18 shows a comparison of the Vs30–Z1.0 relation for California (blue dash line), Japan (green line), and Taiwan (thick black line); furthermore, those equations are
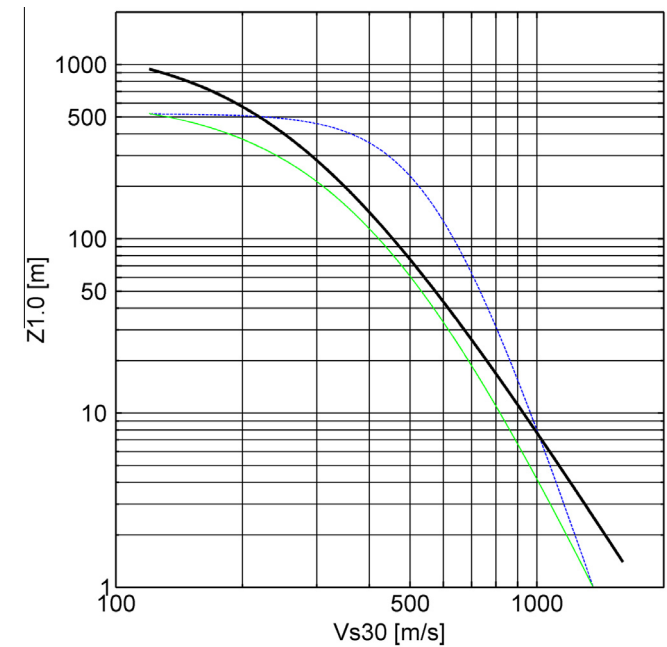
Fig. 18. Comparison of the Vs30–Z1.0 relations for California (blue dash line), Japan (green line), and Taiwan (thick black line). The functional form for Taiwan matches that for Japan but differs with that for California. (For interpretation of the references to color in this figure legend, the reader is referred to the web version of this article.)

Table 1
Functional forms and coefficients of the Vs30–Z1.0 relations for Taiwan, Japan, and California.

| Regions	Functional form	Coefficients		
		a	b	c
Taiwan[a]	$\ln(Z_{1.0}) = \frac{a}{2}\ln\left(\frac{V_{s30}^2 + b^2}{c^2 + b^2}\right)$	−3.8	266	1750
Japan[b]		−5.23	412	1360
California[b]	$\ln(Z_{1.0}) = \frac{a}{4}\ln\left(\frac{V_{s30}^4 + b^4}{c^4 + b^4}\right)$	−7.15	571	1360

[a] This study.
[b] Chiou and Youngs (2014).

listed in Table 1. The relations of Taiwan and Japan are similar. For Vs30 greater than 500 m/s, the rate of decrease in Z1.0 with Vs30 is higher in California than in Japan and Taiwan. Although Z1.0 is larger in Taiwan for soft soil sites, it does not exceed 1000 m in our current database; however, Z1.0 exceeds 1000 m at many sites in South California and Japan (Chiou and Youngs, 2013). The relation may still vary if more Vs30–Z1.0 data are considered.

6. Conclusions

In this study, we attempted to extend the resolution of S-wave velocity profiles to greater than 1000 m/s for depths up to the bedrock as obtained from the microtremor array measurements conducted in the Western Plain of Taiwan. For this purpose, we adopted a two-stage inversion scheme. The first stage is the inversion of phase velocities, which derives the shallow part of the S-wave velocity profiles. The second stage is the inversion of the HVSR, which gives the deep part of the S-wave velocity profiles. The idea is that in the first stage, the S-wave velocity profiles of the shallower parts will be completely derived from the observed phase velocities, which provide information related to both the velocity and the thickness of the layers, while in the second stage, the deeper part of the S-wave velocity profiles can be further estimated from the HVSR, which relates to the sedimentary thickness and the velocity impedance between the sediments and the bedrock. In other words, the second stage of inversion is performed under the condition that the S-wave velocity profile obtained from the first stage is fixed as the shallow part of the initial model for the accurate estimation of the deeper S-wave velocity profile that includes the bedrock. Phase velocities at a higher frequency gave information about shallow subsurface structures, while the HVSR at a lower frequency (especially at the dominant frequency) gave information about deep subsurface structures. S-wave velocity profiles consisting of the bedrock of velocities greater than 1000 m/s were consequently derived for all 45 sites using the proposed
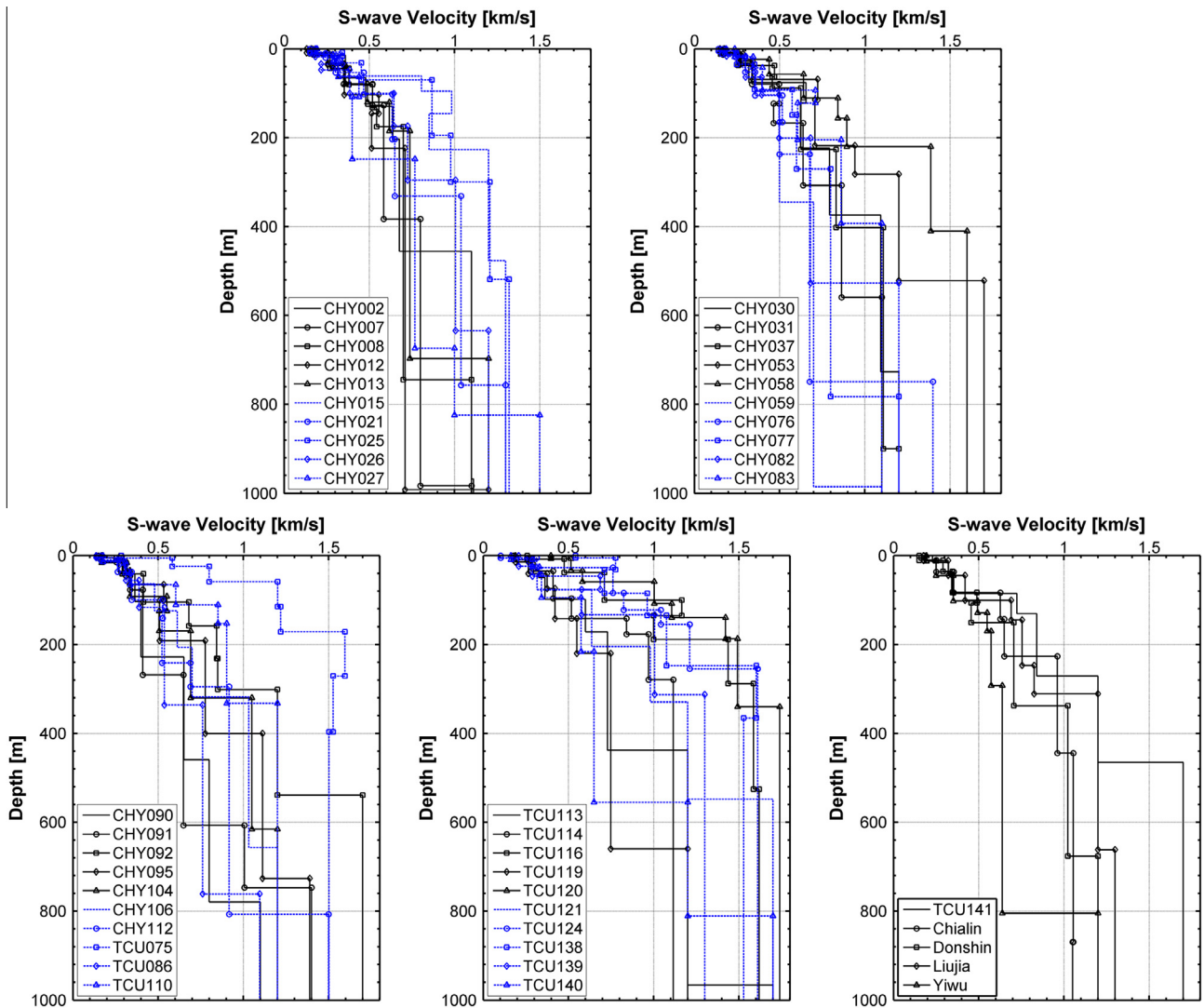
Fig. 19. The final S-wave velocity structures at the 45 sites where microtremor arrays were conducted to derived the models.

two-stage inversion approach. The final S-wave velocity structures at the 45 stations are shown separately in Fig. 19.

We selected previously logged velocity profiles at or near our array measurement sites to compare with our inversion results. The comparisons made at different depth ranges showed highly comparable results, thus confirming that the S-wave velocity profiles derived by the microtremor array measurement method using a two-stage inversion scheme in this study are accurate and highly reliable for a broad depth range. A comparison of Vs30 values obtained from previously logged data and our microtremor array results had a close resemblance. The database of measured Vs30 in this region was updated at three free-field strong-motion stations, i.e., CHY091 (248 m/s), TCU119 (222 m/s), and TCU124 (241 m/s), and 11 other sites. The updated Vs30 map shown in Fig. 13 illustrates the variety of seismic site conditions in the research area.

Furthermore, the contours of two important bedrocks with S-wave velocities of 600 m/s and 1000 m/s obtained from the results of 51 microtremor array measurements of Lin et al. (2009) and this study were compared. The depth of the engineering bedrock for Vs = 600 m/s is approximately 50 m in the piedmont area and approximately 300 m at the coastline. The depth for Vs = 1000 m/s increases from 200 m in the piedmont to approximately 1000 m at the west coast. Previous studies (Chung and Yeh, 1997; Hwang et al., 2003; Wu and Huang, 2013) on this region presented comparable sedimentary thicknesses in the plain and foothill areas. To provide knowledge of the basin depth for ground motion prediction studies, Z1.0 from the present study and Lin et al. (2009) for the sites with Vs30 = 148–604 m/s as well as from the EGDT (Kuo et al., 2012) for the sites with Vs30 = 253–1538 m/s were considered. The distribution property in Taiwan is more similar to that in Japan than in California; thus, the functional form of Japan (Chiou and Youngs, 2013) was selected for Taiwan. The Vs30–Z1.0 relations for Taiwan, Japan, and California clearly showed the similarity between Taiwan and Japan. This might be an implication for similarity in the characteristics of the sedimentary geology of the two regions. In summary, the following are significant results achieved in this study: (1) the updated Vs30 map for the Western Plain of Taiwan using results of both the EGDT and microtremor array measurements; (2) the shallow S-wave velocity structure included the bedrock with a velocity greater than 1000 m/s for the Western Plain of Taiwan; (3) Vs30–Z1.0 data at 87 sites from the microtremor array method and logging method, as well as the relation between Vs30 and Z1.0 for Taiwan, were derived.

References

Abrahamson, N.A., Silva, W.J., 2008. Summary of the Abrahamson & Silva NGA ground-motion relations. Earthquake Spectra 24 (1), 67–97.
Abrahamson, N.A., Silva, W.J., Kamai, R., 2014. Summary of the ASK14 ground motion relation for active crustal regions. Earthquake Spectra 30 (3), 1025–1055.
Aki, K., 1957. Space and time spectra of stationary stochastic waves, with special reference to microtremors. Bull. Earthquake Res. Inst. Tokyo Univ. 35 (3), 415–456.
American Society of Civil Engineers, ASCE, 2010. Minimum Design Loads for Buildings and Other Structures 7–10. American Society of Civil Engineers, Reston, Virginia.
Arai, H., Tokimatsu, K., 2004. S-wave velocity profiling by inversion of microtremors H/V spectrum. Bull. Seismol. Soc. Am. 94 (1), 53–63.
Arai, H., Tokimatsu, K., 2005. S-wave velocity profiling by joint inversion of microtremors dispersion curve and horizontal-to-vertical (H/V) spectrum. Bull. Seismol. Soc. Am. 95 (5), 1766–1778.
Boore, D.M., Stewart, J.P., Seyhan, E., Atkinson, G.A., 2014. NGA-West2 equations for predicting PGA, PGV, and 5% damped PSA for shallow crustal earthquakes. Earthquake Spectra 30 (3), 1057–1085.
Building Seismic Safety Council, BSSC, 2004. NEHRP Recommended Provisions for Seismic Regulations for New Buildings and Other Structures (FEMA 450), 2003 edition. National Institute of Building Sciences, Washington, DC.
Capon, J., 1969. High-resolution frequency-wavenumber spectrum analysis. Proc. IEEE 57 (8), 1408–1418.
Castellaro, S., Mulargia, F., Rossi, P.L., 2008. Vs30: proxy for seismic amplification? Seismol. Res. Lett. 79, 540–543.
Central Geological Survey, 2007. The Subsurface Geological and Engineering Environmental Survey and Research in Taichung, Changhua, Yunlin, Chiayi, and Pingtung Metropolitans Report of the Central Geological Survey, No. 96-18 (in Chinese).
Central Geological Survey, 2010. Active Fault Map of Taiwan 2010.
Chen, C.T., Kuo, C.H., Wen, K.L., Lin, C.M., Huang, J.Y., in press. Simulating the shallow soil response by numerical modeling of wave propagation in the western plain of Taiwan. Terr. Atmos. Oceanic Sci. 27 (3), 359–373.
Cheng, S.N., Yeh, Y.T., Hsu, M.T., Shin, T.C., 1999. Atlas of the Ten Disastrous Earthquakes in Taiwan. Central Weather Bureau, Taiwan (In Chinese).
Chiou, B.S.J., Youngs, R.R., 2008. NGA Model for Average Horizontal Component of Peak Ground Motion and Response Spectra PEER Report 2008/09. University of California, Berkeley.
Chiou, B.S.J., Youngs, R.R., 2013. Update of the Chiou and Youngs NGA Ground Motion Model for Average Horizontal Component of Peak Ground Motion and Response Spectra PEER Report 2013/07. University of California, Berkeley.
Chiou, B.S.J., Youngs, R.R., 2014. Update of the Chiou and Youngs NGA Model for the Average Horizontal Component of Peak Ground Motion and Response Spectra. Earthquake Spectra 30 (3), 1117–1153.
Chung, J.K., Yeh, Y.T., 1997. Shallow crustal structure from short-period rayleigh-wave dispersion data in southwestern Taiwan. Bull. Seismol. Soc. Am. 87 (2), 370–382.
Fäh, D., Kind, F., Giardini, D., 2003. Inversion of local S-wave velocity structures from average H/V ratios, and their use for the estimation of site-effects. J. Seismolog. 7, 449–467.
Field, E., Jacob, K., 1993. The theoretical response of sedimentary layers to ambient noise. Geophys. Res. Lett. 20 (24), 2925–2928.
García-Jerez, A., Luzon, F., Navarro, M., Perez-Ruiz, J.A., 2006. Characterization of the sedimentary cover of the Zafarraya Basin, Southern Spain, by means of ambient noise. Bull. Seismol. Soc. Am. 96 (5), 1915–1933.
García-Jerez, A., Navarro, M., Alcala, F.J., Luzon, F., Perez-Ruiz, J.A., Enomoto, T., Vidal, F., Ocana, E., 2007. Shallow velocity structure using joint inversion of array and h/v spectral ratio of ambient noise: the case of Mula town (SE of Spain). Soil Dynam. Earthquake Eng. 27, 907–919.
Giulio, G.D., Cornou, C., Ohrnberger, M., Wathelet, M., Rovelli, A., 2006. Deriving wavefield characteristics and shear-velocity profiles from two-dimensional small-aperture arrays analysis of ambient vibrations in a small-size alluvial basin, Colfiorito, Italy. Bull. Seismol. Soc. Am. 96 (5), 1915–1933.
Guillier, B., Chatelain, J.L., Hellel, M., Machane, D., Mezouer, N., Salem, R.B., Oubaiche, E.H., 2005. Smooth bumps in H/V curves over a broad area from single-station ambient noise recordings are meaningful and reveal the importance of Q in array processing: the Boumerdes (Algeria) case. Geophys. Res. Lett. 32, L24306.
Haskell, N.A., 1960. Crustal reflection of plane SH waves. J. Geophys. Res. 65, 4147–4150.
Herrmann, R.B., 1985. Computer Programs in Seismology. Saint Louis University.
Herrmann, R.B., 1987. Surface wave inversion. Computer Program in Seismology, vol. 4. Saint Louis University, p. 104 pp.
Ho, C.S., 1988. An Introduction to the Geology of Taiwan: Explanatory Text for the Geologic Map of Taiwan. Ministry of Economic Affairs, Taipei, Taiwan, second ed.
Horike, M., 1985. Inversion of phase velocity of long-period microtremors to the S-wave velocity structure down to the basement in urbanized areas. J. Phys. Earth 33, 59–96.
Hu, J.C., Liu, C.C., Yang, T.Y.F., Chin, K.E., Cheng, C.T., 2015. Monitoring and potential analysis of faults. In: Workshop of the Executive Yuan Science and Technology Program Results for Disaster Prevention and Relief and International Disaster and Risk Management Seminar, Taipei, Taiwan.
Hwang, R.D., Yu, G.K., Chang, W.Y., Chang, J.P., 2003. Lateral variations of shallow shear-velocity structure in southwestern Taiwan inferred from short-period Rayleigh waves. Earth Planets Space 55, 349–354.
Kawase, H., Satoh, T., Iwata, T., Irikura, K., 1998. S-wave velocity structure in the San Fernando and Santa Monica areas. Proceedings of the 2nd International Symposium on the Effects of Surface Geology on Seismic Motion, vol. 2, pp. 733–740.

Kudo, K., Kanno, T., Okada, H., Ozel, O., Erdik, M., Sasatani, T., Higashi, S., Takahashi, M., Yoshida, K., 2002. Site-specific issues for strong ground motions during the Kocaeli, Turkey, earthquake of 17 August 1999, as inferred from array observations of microtremors and aftershocks. Bull. Seismol. Soc. Am. 92 (1), 448–465.

Kuo, C.H., Cheng, D.S., Hsieh, H.H., Chang, T.M., Chiang, H.J., Lin, C.M., Wen, K.L., 2009. Comparison of three different methods in investigating shallow shear-wave velocity structures in Ilan, Taiwan. Soil Dynam. Earthquake Eng. 29 (1), 133–143.

Kuo, C.H., Wen, K.L., Hsieh, H.H., Chang, T.M., Lin, C.M., Chen, C.T., 2011. Evaluating empirical regression equations for Vs and estimating Vs30 in Northeastern Taiwan. Soil Dynam. Earthquake Eng. 31 (3), 431–439.

Kuo, C.H., Wen, K.L., Hsieh, H.H., Lin, C.M., Chang, T.M., Kuo, K.W., 2012. Site classification and Vs30 estimation of free-field TSMIP stations using the logging data of EGDT. Eng. Geol. 129–130, 68–75.

Kuo, C.H., Wen, K.L., Lin, C.M., Wen, S., Huang, J.Y., 2015. Investigating near surface S-wave velocity properties using ambient noise in southwestern Taiwan. Terr. Atmos. Oceanic Sci. 26 (2), 205–211.

Lee, S.J., Chen, H.W., Huang, B.S., 2008. Simulations of strong ground motion and 3D amplification effect in the Taipei Basin by using a composite grid finite-difference method. Bull. Seismol. Soc. Am. 98 (3), 1229–1242.

Lermo, J., Chavez-Garcia, F.J., 1993. Site effect evaluation using spectral ratios with only one station. Bull. Seismol. Soc. Am. 83 (5), 1574–1594.

Lin, C.M., 2009. Shallow Velocity Structure, Site Effect and 3D Seismic Wave Simulation of the Western Plain of Taiwan Ph.D. Thesis. Institute of Geophysics, National Central University, Taiwan, p. 142 pp (In Chinese).

Lin, C.M., Chang, T.M., Huang, Y.C., Chiang, H.J., Kuo, C.H., Wen, K.L., 2009. Shallow S-wave velocity structures in the western coastal plain of Taiwan. Terr. Atmos. Oceanic Sci. 20 (2), 299–308.

Lin, C.M., Wen, K.L., Kuo, C.H., Lin, C.Y., 2014. S-wave velocity model of taipei basin. In: Proceeding of the 5th Asia Conference on Earthquake Engineering, Taipei, Taiwan.

Louie, J.N., 2001. Faster, better: shear-wave velocity to 100 m depth from refraction microtremors arrays. Bull. Seismol. Soc. Am. 91 (2), 347–364.

Matsushima, T., Okada, H., 1990. Determination of deep geological structures under urban areas using long-period microtremors. Butsuri Tansa 43, 21–33.

Meng, C.Y., 1968. Geologic concepts relating to the petroleum prospects of Taiwan Strait. Petrol. Geol. Taiwan 6, 1–13.

Nakamura, Y., 1989. A method for dynamic characteristics estimation of subsurface using microtremors on the ground surface. Quart. Rep. Railway Tech. Res. Inst. 30 (1), 25–33.

Nakamura, Y., 2007. Characteristics of H/V spectrum. In: NATO Advanced Research Workshop, Dobrovnik, Croatia.

Nardone, L., Maresca, R., 2011. Shallow velocity structure and site effects at Mt. Vesuvius, Italy, from HVSR and array measurements of ambient vibrations. Bull. Seismol. Soc. Am. 101 (4), 1465–1477.

Ohori, M., Nobata, A., Wakamatsu, K., 2002. A comparison of ESAC and FK methods of estimating phase velocity using arbitrarily shaped microtremors arrays. Bull. Seismol. Soc. Am. 92 (6), 2323–2332.

Pancha, A., Anderson, J.G., Louie, J.N., Pullammanappallil, S.K., 2008. Measurement of shallow shear wave velocities at a rock site using the ReMi technique. Soil Dynam. Earthquake Eng. 28, 522–535.

Parolai, S., Picozzi, M., Richwalski, S.M., Milkereit, C., 2005. Joint inversion of phase velocity dispersion and H/V ratio curves from seismic noise recordings using a genetic algorithm, considering higher modes. Geophys. Res. Lett. 32 (1), L01303.

Picozzi, M., Parolai, S., Richwalski, S.M., 2005. Joint inversion of H/V ratios and dispersion curves from seismic noise: estimating the S-wave velocity of bedrock. Geophys. Res. Lett. 32, L11308.

Raptakis, D., Makra, K., 2010. Shear wave velocity structure in western Thessaloniki (Greece) using mainly alternative SPAC method. Soil Dynam. Earthquake Eng. 30, 202–214.

Rau, R.J., Ma, K.F., Chan, C.H., Shyu, J.B.H., Cheng, S.N., Wen, K.L., Lee, Y.H., Lee, S.J., 2015. Taiwan earthquake model: seismic hazard evaluation, artificial earthquake test, and seismic risk. In: Workshop of the Executive Yuan Science and Technology Program Results for Disaster Prevention and Relief and International Disaster and Risk Management Seminar, Taipei, Taiwan.

Sato, T., Kawase, H., Matsui, M., Kataoka, S., 1991. Array measurement of high frequency microtremors for underground structure estimation. Proceedings of 4th International Conference on Seismic Zonation, vol. 2, pp. 409–416.

Satoh, T., Kawase, H., Iwata, T., Higashi, S., Sato, T., Irikura, K., Huang, H.C., 2001a. S-wave velocity structure of the Taichung Basin, Taiwan, estimated from array and single-station records of microtremors. Bull. Seismol. Soc. Am. 91 (5), 1267–1282.

Satoh, T., Kawase, H., Matsushima, S., 2001b. Estimation of S-wave velocity structures in and around the Sendai Basin, Japan, using array records of microtremors. Bull. Seismol. Soc. Am. 91 (2), 206–218.

Shin, T.C., Chang, C.H., Pu, H.C., Lin, H.W., Leu, P.L., 2013. The geophysical database management system in Taiwan. Terr. Atmos. Oceanic Sci. 24, 11–18.

Sun, S.C., 1982. The tertiary basins of offshore Taiwan. In: Proceedings of Second ASCOPT Conference and Exhibition, Manila, Philippine, pp. 126–135.

Wathelet, M., Johnmans, D., Ohrnberger, M., 2004. Surface-wave inversion using a direct search algorithm and its application to ambient vibration measurements. Near Surf. Geophys. 2 (4), 211–221.

Wen, K.L., Kuo, C.H., Chang, S.C., Leu, P.L., Chiang, C.H., Lin, B.Y., 2014. The Analysis of Site-effect for CWB Surface-Downhole Stations. CWB Annual Reports 63, MOTC-CWB-103-E-07 (In Chinese with English abstract).

Wu, C.F., Huang, H.C., 2012. Estimation of shallow S-wave velocity structure in the Puli basin, Taiwan, using array measurements of microtremors. Earth Planets Space 64, 389–403.

Wu, C.F., Huang, H.C., 2013. Near-surface shear-wave velocity structure of the Chiayi area, Taiwan. Bull. Seismol. Soc. Am. 103 (2A), 1154–1164.

Yamanaka, H., Ishida, H., 1996. Application of genetic algorithms to an inversion of surface-wave dispersion data. Bull. Seismol. Soc. Am. 86, 436–444.